CrossMark

JM PAPERS

Stokesian motion of a spherical particle near a right corner made by tangentially moving walls

Francesco Romanò[1],†, Pierre-Emmanuel des Boscs[2] and Hendrik C. Kuhlmann[2]

[1]UMR 9014 - LMFL - Laboratoire de Mécanique des Fluides de Lille - Kampé de Fériet, Univ. Lille, CNRS, ONERA, Arts et Métiers Institute of Technology, Centrale Lille, F-59000 Lille, France

[2]Institute of Fluid Mechanics and Heat Transfer, TU Wien, Getreidemarkt 9, 1060 Vienna, Austria

The slow motion of a small buoyant sphere near a right dihedral corner made by tangentially sliding walls is investigated. Under creeping-flow conditions the force and torque on the sphere can be decomposed into eleven elementary types of motion involving simple particle translations, particle rotations and wall movements. Force and torque balances are employed to find the velocity and rotation of the particle as functions of its location. Depending on the ratio of the wall velocities and the gravitational settling velocity of the sphere, different dynamical regimes are identified. In particular, a non-trivial line attractor/repeller for the particle motion exists at a location detached from both the walls. The existence, location and stability of the corresponding two-dimensional fixed point are studied depending on the wall velocities and the buoyancy force. The impact of the line attractors/repellers on the motion of small particles in cavities and its relevance for corner cleaning applications are discussed.

Key words: Stokesian dynamics, microfluidics, particle/fluid flow

1. Introduction

Small particles suspended in an incompressible fluid are frequently employed in microfluidic systems (Lenshof & Laurell 2010), drug delivery (Edwards *et al.* 1997) and lab-on-a-chip devices (Wang & Zhe 2011). The flow in these confined systems is typically characterised by small length and velocity scales. It is, therefore, essential to investigate the particle dynamics for small particle Reynolds numbers, usually approximated as Stokesian, with a focus on the interaction of a particle with rigid or deformable boundaries, e.g. with other particles, walls and fluid–fluid interfaces.

† Email address for correspondence: francesco.romano@ensam.eu

927 A41-1

Since the pioneering work of Lorentz (1907), who investigated the motion of a sphere towards a distant rigid wall, several other authors considered similar problems, including a particle rotating parallel or tangent to a plane wall (Jeffery 1915; Goldman, Cox & Brenner 1967*a*), two particles moving towards each other (Stimson & Jeffery 1926), a particle moving towards a plane surface (either a wall or a free surface, see e.g. Brenner (1961)), parallel to a wall (Faxén 1927) or in a shear flow (Goldman, Cox & Brenner 1967*b*). A comprehensive overview of all such fundamental flows involving particle–wall interactions is provided by Chaoui & Feuillebois (2003), who discuss the exact solutions, whenever available, and the matching of various asymptotic regimes (lubrication approximation) for a particle moving far from or near a plane wall. These studies include tabulated results derived by numerical approximations, analytical solutions and asymptotic expansions that characterise the augmentation of the Stokes drag and torque on the particle due to the presence of a nearby boundary. Since all these investigations imply Stokes flow, the near-boundary corrections to the classical drag and torque for a particle in an unbounded domain can be superimposed to compute the particle dynamics near a wall, a free surface or another particle (Chaoui & Feuillebois 2003). A generalisation of the particle–wall interaction which takes into account the wall curvature has recently been reported in Papavassiliou & Alexander (2017). Other generalisations, applicable in the creeping-flow regime, include the effect of a parabolic shear stress near a slip (Feuillebois *et al.* 2011) or no-slip wall (Yahiaoui & Feuillebois 2010). The parabolic part of the velocity profile gives rise to a lift force, which is absent in the creeping-flow approximation when the velocity field near the boundary is expanded only up to linear order (Goldman *et al.* 1967*b*). Other generalisations of the classical problems take into account forces acting on a particle moving near a Brinkman medium. Damiano *et al.* (2004) have shown that the boundary-induced force and torque corrections to those acting in an unbounded domain reduce significantly when the dimensionless permeability of the Brinkman medium is increased.

Common simplifying assumptions concern (i) the creeping-flow approximation, eventually extended to include weak inertia effects via asymptotic expansions (see e.g. Cox & Mason 1971), and (ii) perfectly smooth symmetric surfaces (planar, cylindrical or spherical) of the interacting solid bodies. A step towards more general geometries has recently been made by Dauparas & Lauga (2018), who investigated the Stokes flow past a sphere moving far from a stationary dihedral corner of arbitrary angle. Romanò, des Boscs & Kuhlmann (2020*a*) further extended the results of Dauparas & Lauga (2018) considering a particle near a right dihedral corner between a stationary and a tangentially sliding wall, i.e. near a singular corner.

The main focus of all these studies was directed on the forces and torques exerted by the surrounding fluid on the particle due to the presence of a boundary, either a wall, a free surface or other particles. Such forces and torques become increasingly important the closer the particle approaches the boundary. The presence of a boundary can strongly affect the particle trajectory (Kuehn, Romanò & Kuhlmann 2018): in two-dimensional recirculating flows, the boundary effect can cause limit cycles of the particle motion if the flow is driven by moving walls (Romanò & Kuhlmann 2016) or by a constant (Romanò & Kuhlmann 2017) or a variable shear stress along a free surface (Orlishausen *et al.* 2017; Romanò *et al.* 2017). In laminar micro- or millimetric three-dimensional flows, the particle–boundary interaction may lead to non-trivial accumulation phenomena such as finite-size Lagrangian coherent structures which have been observed experimentally (Schwabe, Hintz & Frank 1996; Kuhlmann *et al.* 2016; Romanò, Wu & Kuhlmann 2019*b*; Wu, Romanò & Kuhlmann 2021) and computed numerically (Hofmann & Kuhlmann 2011; Mukin & Kuhlmann 2013; Muldoon & Kuhlmann 2013; Romanò & Kuhlmann 2018;
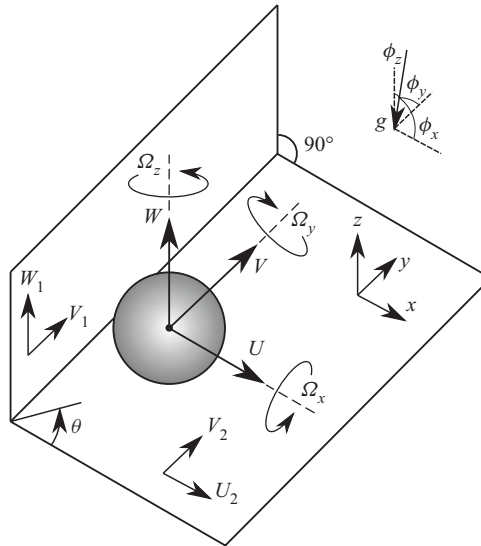
Figure 1. Sketch of the general problem: a sphere moving in Stokes flow near a semi-infinite right dihedral corner made by two moving walls.

Romanò, Kunchi Kannan & Kuhlmann 2019a) for boundary-driven flows. We refer to Romanò & Kuhlmann (2019) for a corresponding review. The forces of interaction between a particle and a confining surface also play an important role in applications such as particle trapping (Donolato *et al.* 2009), particle sorting (Karimi, Yazdi & Ardekani 2013) or corner cleaning, which is crucial for several micro- and nanofluidic devices.

In this study we use the forces and torques on a sphere in Stokes flow numerically computed by Romanò *et al.* (2020a) for a right dihedral corner to construct the force and torque fields for more general wall motions. Taking into account buoyancy forces, the trapping of a small particle near a right dihedral corner is investigated. As near-corner corrections to the forces and torques exerted on a particle have become available only recently, our study aims at investigating the boundary effect on the near-corner particle dynamics, eventually uncovering a counter-intuitive trapping phenomenon for inertialess particles. The paper is structured as follows. Section 2 formulates the mathematical problem. In § 3 the particle translational and rotational velocities are obtained by balancing forces and torques at the particle centroid. The particle dynamics is analysed in § 4, while § 5 summarises the results and draws conclusions.

2. Problem formulation

A rigid spherical particle moves with translational and rotational velocity $\tilde{U} = (\tilde{U}, \tilde{V}, \tilde{W})$ and $\tilde{\Omega} = (\tilde{\Omega}_x, \tilde{\Omega}_y, \tilde{\Omega}_z)$, respectively, near a semi-infinite dihedral corner. The sphere has radius a_p and density ρ_p. The surrounding fluid is Newtonian with constant density ρ_f and kinematic viscosity ν. The dihedral corner is formed by two orthogonal plane walls at $\tilde{x} = 0$ (wall 1) and $\tilde{z} = 0$ (wall 2), hence the corner edge is located at $\tilde{x} = (0, \tilde{y}, 0)$. Both walls move tangentially in their own planes, but with different velocities $\tilde{U}_1 = (0, \tilde{V}_1, \tilde{W}_1)$ and $\tilde{U}_2 = (\tilde{U}_2, \tilde{V}_2, 0)$ for wall 1 and wall 2, respectively. Owing to the density difference $\Delta\rho = \rho_p - \rho_f$ between particle and fluid and the gravitational acceleration $\mathbf{g} = g(\cos\phi_x, \cos\phi_y, \cos\phi_z)$, buoyancy affects the motion of the sphere, with ϕ_x, ϕ_y and ϕ_z being the yaw, pitch and roll angles the vector $\mathbf{g}$ makes with the axes $(\tilde{x}, \tilde{y}, \tilde{z})$ of the Cartesian coordinate system, such that $\cos^2\phi_x + \cos^2\phi_y + \cos^2\phi_z = 1$ (figure 1).

Variable	$\tilde{x}, \tilde{x}_p, \tilde{x}_s$	$\tilde{U}, \tilde{U}_1, \tilde{U}_2$	$\tilde{\boldsymbol{\Omega}}$	$\tilde{p}$
Scale	a_p	ν/a_p	ν/a_p^2	$\rho_f \nu^2/a_p^2$

Table 1. Scaling of the dimensional variables.

Let us consider a finite region of length scale L in the vicinity of the corner such that the Reynolds numbers of the global flow $\tilde{u}$ in this region will be small with $Re_1 = |\tilde{U}_1|L/\nu \ll 1$ and $Re_2 = |\tilde{U}_2|L/\nu \ll 1$. We also assume a small local particle Reynolds number $\widehat{Re}_p = |\tilde{U} + \tilde{\boldsymbol{\Omega}} \times (\tilde{x}_s - \tilde{x}_p) - \tilde{u}|a_p/\nu \ll 1$, where $\tilde{x}_s$ and $\tilde{x}_p = (\tilde{x}_p, \tilde{y}_p, \tilde{z}_p)$ denote the position vectors of the particle's surface and centroid, respectively. In this case, the inertial term in the Navier–Stokes equation can be neglected and the incompressible flow past the particle can be described by Stokes flow.

Scaling length, velocity and pressure by a_p, ν/a_p and $\rho_f \nu^2/a_p^2$ (table 1), respectively, and dropping the tilde for all non-dimensional quantities, the continuity and momentum equations read

$$\nabla \cdot \boldsymbol{u} = 0, \quad \nabla p = \nabla^2 \boldsymbol{u}, \tag{2.1a,b}$$

where $\boldsymbol{u}$ and p are the non-dimensional fluid velocity and reduced pressure fields, respectively. The flow field must satisfy the no-slip boundary conditions on the walls and the surface of the particle:

$$x = 0: \quad \boldsymbol{u} = U_1, \tag{2.2a}$$

$$z = 0: \quad \boldsymbol{u} = U_2, \tag{2.2b}$$

$$x = x_s: \quad \boldsymbol{u} = U + \boldsymbol{\Omega} \times (x_s - x_p). \tag{2.2c}$$

Considering the particle motion close to the corner edge such that $|x_p| \ll L/a_p$, the effect of the moving sphere on the flow at a distance L/a_p from the corner is vanishingly small. Therefore, the mathematical problem can be closed, as in Romanò *et al.* (2020a), by considering a finite domain bounded at a distance $\sim L/a_p$ from the corner on which the known Stokes flow solution to (2.1a,b) in the absence of the particle in which the flow is driven by the moving walls only (Taylor 1962) is imposed. For the case $U_1 \equiv 0$, the analytic far field at $|x| = O(L/a_p)$ only depends on the polar angle $\theta = \cos^{-1}(x/\sqrt{x^2 + z^2})$:

$$u = U_2 \left[f'(\theta) \cos(\theta) + f(\theta) \sin(\theta) \right], \tag{2.3a}$$

$$v = V_2(1 - 2\theta/\pi), \tag{2.3b}$$

$$w = U_2 \left[f'(\theta) \sin(\theta) - f(\theta) \cos(\theta) \right], \tag{2.3c}$$

where $f(\theta) = [\theta \sin(\pi/2 - \theta) - \pi/2(\pi/2 - \theta) \sin \theta]/(1 - \pi^2/4)$. In case $U_2 \equiv 0$ and $U_1 \neq 0$, the far field is given by (2.3) reflected about the bisector $\theta = \pi/4$ with U_2 replaced by U_1. Finally, owing to the linearity of (2.1a,b), the boundary condition for $U_1 \neq 0$ and $U_2 \neq 0$ is obtained as a linear combination of (2.3) and its mirror-symmetric counterpart.

Owing to the linearity of the Stokes problem, the general problem sketched in figure 1 can be decomposed into eleven cases, illustrated in figure 2, which can be reduced to seven elementary subproblems by symmetry arguments:

(I) a sphere moving parallel to the edge of a stationary corner,

$$U_1 = 0, \quad U_2 = 0, \quad U = Ve_y, \quad \mathbf{\Omega} = 0, \quad g = 0; \qquad (2.4)$$

(II) a sphere rotating about an axis parallel to the edge of a stationary corner,

$$U_1 = 0, \quad U_2 = 0, \quad U = 0, \quad \mathbf{\Omega} = \Omega_y e_y, \quad g = 0; \qquad (2.5)$$

(III) a sphere moving normal to one of the walls of a stationary corner,

$$(a) \quad U_1 = 0, \quad U_2 = 0, \quad U = Ue_x, \quad \mathbf{\Omega} = 0, \quad g = 0, \qquad (2.6)$$

$$(b) \quad U_1 = 0, \quad U_2 = 0, \quad U = We_z, \quad \mathbf{\Omega} = 0, \quad g = 0; \qquad (2.7)$$

(IV) a sphere rotating about an axis normal to one of the walls of a stationary corner,

$$(a) \quad U_1 = 0, \quad U_2 = 0, \quad U = 0, \quad \mathbf{\Omega} = \Omega_x e_x, \quad g = 0, \qquad (2.8)$$

$$(b) \quad U_1 = 0, \quad U_2 = 0, \quad U = 0, \quad \mathbf{\Omega} = \Omega_z e_z, \quad g = 0; \qquad (2.9)$$

(V) a stationary sphere near a corner with one wall moving parallel to the edge,

$$(a) \quad U_1 = V_1 e_y, \quad U_2 = 0, \quad U = 0, \quad \mathbf{\Omega} = 0, \quad g = 0, \qquad (2.10)$$

$$(b) \quad U_1 = 0, \quad U_2 = V_2 e_y, \quad U = 0, \quad \mathbf{\Omega} = 0, \quad g = 0; \qquad (2.11)$$

(VI) a stationary sphere near a corner with one wall moving normal to the edge,

$$(a) \quad U_1 = W_1 e_z, \quad U_2 = 0, \quad U = 0, \quad \mathbf{\Omega} = 0, \quad g = 0, \qquad (2.12)$$

$$(b) \quad U_1 = 0, \quad U_2 = U_2 e_x, \quad U = 0, \quad \mathbf{\Omega} = 0, \quad g = 0; \qquad (2.13)$$

(VII) and a stationary sphere near a stationary corner subject to a gravitational field,

$$U_1 = 0, \quad U_2 = 0, \quad U = 0, \quad \mathbf{\Omega} = 0, \quad g = ga^3/v^2(\cos\phi_x, \cos\phi_y, \cos\phi_z); \qquad (2.14)$$

where the velocities of the walls and the sphere, i.e. U_1, U_2 and U, have already been non-dimensionalised by v/a_p, the particle rotation rate $\mathbf{\Omega}$ is normalised by v/a_p^2, and the acceleration due to gravity g is scaled by v^2/a_p^3.

3. Dynamics of a sphere free to translate and rotate

Owing to the quasi-steady motion holding under the creeping-flow approximation, the resultant of forces and torques on the particle must be null. The corresponding balances can be expressed by superimposing forces and torques which arise due to the subproblems illustrated in figure 2. In terms of force and torque coefficients $F = (F_x, F_y, F_z)$ and $T = (T_x, T_y, T_z)$, i.e. forces and torques scaled by the Stokes drag $6\pi\rho_f v a_p U$ and the couple $8\pi\rho_f v a_p^2 U$, respectively, the force and torque balances are linear in $U = (U, V, W)$ and $\mathbf{\Omega} = (\Omega_x, \Omega_y, \Omega_z)$, respectively, and can be written in the form

$$
\begin{pmatrix}
F_x^{IIIa} & 0 & F_x^{IIIb} & 0 & F_x^{II} & 0 \\
0 & F_y^{I} & 0 & F_y^{IVa} & 0 & F_y^{IVb} \\
F_z^{IIIa} & 0 & F_z^{IIIb} & 0 & F_z^{II} & 0 \\
0 & T_x^{I} & 0 & T_x^{IVa} & 0 & T_x^{IVb} \\
T_y^{IIIa} & 0 & T_y^{IIIb} & 0 & T_y^{II} & 0 \\
0 & T_z^{I} & 0 & T_z^{IVa} & 0 & T_z^{IVb}
\end{pmatrix}
\cdot
\begin{pmatrix}
U \\
V \\
W \\
\Omega_x \\
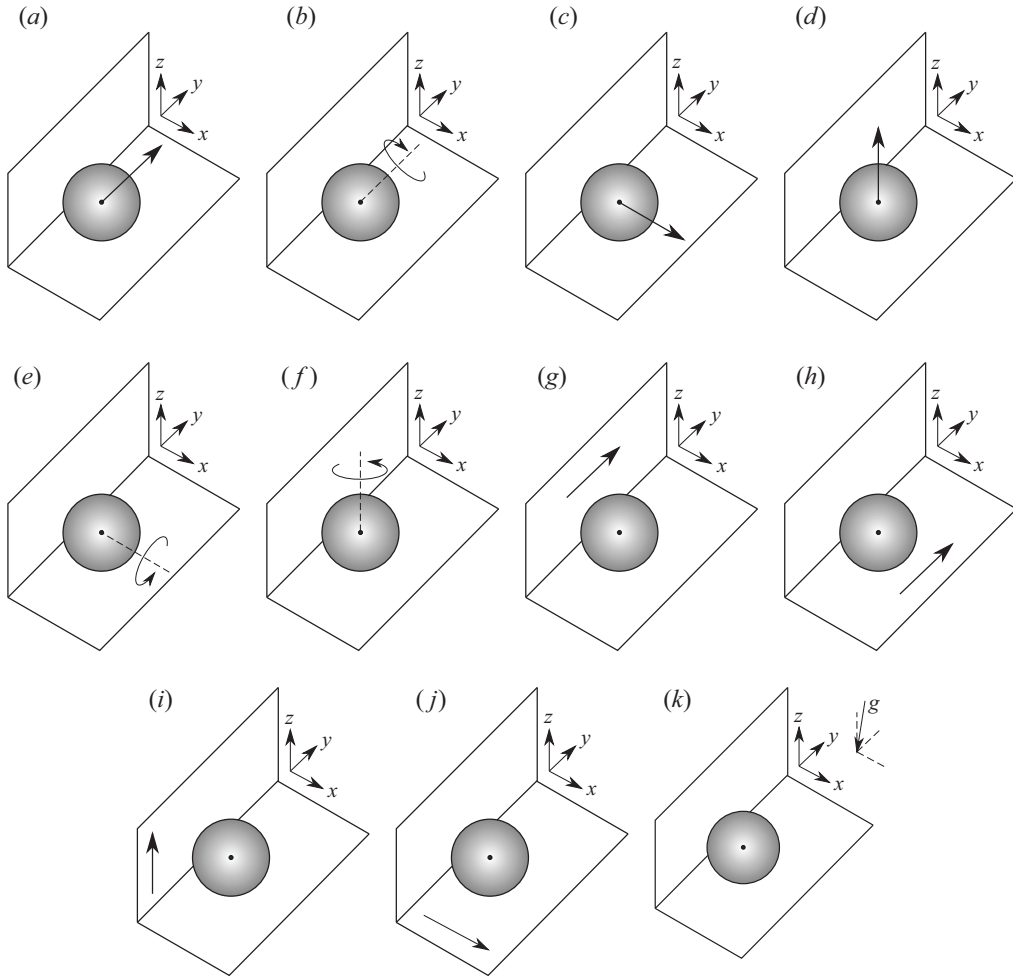\Omega_y \\
\Omega_z
\end{pmatrix}
$$

Figure 2. Decomposition of the general problem into elementary subproblems: (*a*) problem I, (*b*) problem II, (*c*) problem IIIa, (*d*) problem IIIb, (*e*) problem IVa, (*f*) problem IVb, (*g*) problem Va, (*h*) problem Vb, (*i*) problem VIa, (*j*) problem VIb and (*k*) problem VII. The arrows show the translational and rotational motions.

$$+\begin{pmatrix} W_1 F_x^{VIa} & + & U_2 F_x^{VIb} & + & (2/9)(1-\varrho)Fr^{-2}\cos\phi_x \\ V_1 F_y^{Va} & + & V_2 F_y^{Vb} & + & (2/9)(1-\varrho)Fr^{-2}\cos\phi_y \\ W_1 F_z^{VIa} & + & U_2 F_z^{VIb} & + & (2/9)(1-\varrho)Fr^{-2}\cos\phi_z \\ V_1 T_x^{Va} & + & V_2 T_x^{Vb} & & \\ W_1 T_y^{VIa} & + & U_2 T_y^{VIb} & & \\ V_1 T_z^{Va} & + & V_2 T_z^{Vb} & & \end{pmatrix} = 0, \qquad (3.1)$$

where the superscript of the force and torque coefficients indicates the respective subproblem from figure 2(*a–k*), $\varrho = \rho_p/\rho_f$ is the particle-to-fluid density ratio, and $Fr = v/\sqrt{ga_p^3}$ is the Froude number. Hence, $U_g = (2/9)(1-\varrho)Fr^{-2} = 2(1-\varrho)ga_p^3/9v^2$ is the non-dimensional settling velocity which is positive if $\varrho < 1$ and negative if $\varrho > 1$.

927 A41-6

The force and torque coefficients in (3.1) only depend on the position x_p of the particle. For the above elementary subproblems (I) to (VI), the forces and torques on the sphere as functions of the sphere's position have recently been computed on a dense grid by Romanò *et al.* (2020*a*) using fully resolving spectral-element simulations. By test calculations and selecting the length L/a_p to be sufficiently large, Romanò *et al.* (2020*a*) have ensured that the results obtained for the force and torque coefficients have become independent of the length L/a_p selected for the computational domain. The numerical data for the force and torque coefficients obtained were fitted by closed-form expressions, which account for the symmetries of each problem as well as for its exact and asymptotic lubrication solutions valid near the walls and far away from the corner edge. As a result, the dependence of the forces and torques on x_p and z_p was characterised.

With the fit functions of Romanò *et al.* (2020*a*) available, (3.1) can be solved to obtain explicit expressions for the velocity and rotation rate of the sphere. Exploiting the structure of the left-hand side of (3.1), one can split the linear system of six equations into two linear systems of three equations each:

$$\underbrace{\begin{pmatrix} F_x^{IIIa} & F_x^{IIIb} & F_x^{II} \\ F_z^{IIIa} & F_z^{IIIb} & F_z^{II} \\ T_y^{IIIa} & T_y^{IIIb} & T_y^{II} \end{pmatrix}}_{:=M_1} \cdot \begin{pmatrix} U \\ W \\ \Omega_y \end{pmatrix} = - \begin{pmatrix} W_1 F_x^{VIa} + U_2 F_x^{VIb} + (2/9)(1-\varrho)Fr^{-2}\cos\phi_x \\ W_1 F_z^{VIa} + U_2 F_z^{VIb} + (2/9)(1-\varrho)Fr^{-2}\cos\phi_z \\ W_1 T_y^{VIa} + U_2 T_y^{VIb} \end{pmatrix}$$

$$= -(A_1 \quad A_2 \quad A_3)^{\mathrm{T}}, \tag{3.2a}$$

$$\underbrace{\begin{pmatrix} F_y^{I} & F_y^{IVa} & F_y^{IVb} \\ T_x^{I} & T_x^{IVa} & T_x^{IVb} \\ T_z^{I} & T_z^{IVa} & T_z^{IVb} \end{pmatrix}}_{:=M_2} \cdot \begin{pmatrix} V \\ \Omega_x \\ \Omega_z \end{pmatrix} = - \begin{pmatrix} V_1 F_y^{Va} + V_2 F_y^{Vb} + (2/9)(1-\varrho)Fr^{-2}\cos\phi_y \\ V_1 T_x^{Va} + V_2 T_x^{Vb} \\ V_1 T_z^{Va} + V_2 T_z^{Vb} \end{pmatrix}$$

$$= -(B_1 \quad B_2 \quad B_3)^{\mathrm{T}}. \tag{3.2b}$$

The solutions of the two linear systems read

$$\begin{pmatrix} U \\ W \\ \Omega_y \end{pmatrix} = \alpha_1 \begin{pmatrix} F_z^{II} T_y^{IIIb} - F_z^{IIIb} T_y^{II} \\ F_z^{IIIa} T_y^{II} - F_z^{II} T_y^{IIIa} \\ F_z^{IIIb} T_y^{IIIa} - F_z^{IIIa} T_y^{IIIb} \end{pmatrix} + \alpha_2 \begin{pmatrix} F_x^{IIIb} T_y^{II} - F_x^{II} T_y^{IIIb} \\ F_x^{II} T_y^{IIIa} - F_x^{IIIa} T_y^{II} \\ F_x^{IIIa} T_y^{IIIb} - F_x^{IIIb} T_y^{IIIa} \end{pmatrix}$$

$$+ \alpha_3 \begin{pmatrix} F_x^{II} F_z^{IIIb} - F_x^{IIIb} F_z^{II} \\ F_x^{IIIa} F_z^{II} - F_x^{II} F_z^{IIIa} \\ F_x^{IIIb} F_z^{IIIa} - F_x^{IIIa} F_z^{IIIb} \end{pmatrix}, \tag{3.3a}$$

$$\begin{pmatrix} V \\ \Omega_x \\ \Omega_z \end{pmatrix} = \beta_1 \begin{pmatrix} T_x^{IVb} T_z^{IVa} - T_x^{IVa} T_z^{IVb} \\ T_x^{I} T_z^{IVb} - T_x^{IVb} T_z^{I} \\ T_x^{IVa} T_z^{I} - T_x^{I} T_z^{IVa} \end{pmatrix} + \beta_2 \begin{pmatrix} F_y^{IVa} T_z^{IVb} - F_y^{IVb} T_z^{IVa} \\ F_y^{IVb} T_z^{I} - F_y^{I} T_z^{IVb} \\ F_y^{I} T_z^{IVa} - F_y^{IVa} T_z^{I} \end{pmatrix}$$

$$+ \beta_3 \begin{pmatrix} F_y^{IVb} T_x^{IVa} - F_y^{IVa} T_x^{IVb} \\ F_y^{I} T_x^{IVb} - F_y^{IVb} T_x^{I} \\ F_y^{IVa} T_x^{I} - F_y^{I} T_x^{IVa} \end{pmatrix}, \tag{3.3b}$$

where $\alpha_i = A_i/\det(\boldsymbol{M}_1)$ and $\beta_i = B_i/\det(\boldsymbol{M}_2)$, with $\boldsymbol{M}_1$ and $\boldsymbol{M}_2$ as defined in (3.2). This form of the balance equations enables a direct computation of the motion of the sphere based on the fit functions provided by Romanò *et al.* (2020*a*).

4. Results

4.1. *Existence of an attractor*

While the velocity field $\boldsymbol{u}$ of the fluid according to (2.1*a*,*b*) is solenoidal and does not exhibit sources or sinks, the velocity field $\boldsymbol{U}$ of the particle according to (3.3) is not solenoidal. In particular, the linear dynamical system $\dot{\boldsymbol{x}}_p = \boldsymbol{U}(\boldsymbol{x}_p)$ governing the motion of the particle centroid may exhibit stationary points which could arise as sinks or sources. Owing to the linearity of the problem, every particle attractor turns into a particle repeller if the direction of the motion of the walls and of the gravity vector is reversed. Here we target the existence and characterisation of stationary points of the particle velocity field $\boldsymbol{U}$.

Due to the symmetry of the problem, the forces and torques acting on the particle are independent of y. Hence, the translational and rotational velocities of the particle are invariant in y, and the dynamics is a superposition of a trivial one-dimensional dynamics in y and a two-dimensional dynamics in the (x, z) plane. Since $\nabla \cdot \boldsymbol{U} = \partial_x U + \partial_z W \neq 0$ attractors/repellers may exists in the (x, z) plane. This implies the particle flow field admits critical lines parallel to the corner edge. Finally, since any critical line only depends on U and W, we only need to consider the parameters affecting the forces acting in the (x, z) plane, i.e. the settling velocity U_g, the z-component W_1 of the velocity of wall 1, the x-component U_2 of the velocity of wall 2, and the angles ϕ_x and ϕ_z the acceleration of gravity makes with the x and z axes, respectively.

Without loss of generality we use the normalisation $U_2 = -1$ and set $\phi_y = 90°$. In this case $\phi_z = 90° - \phi_x$ and the remaining parameter space is made by (W_1, ϕ_x, U_g). Therefore, we screen the particle dynamics on the grid $W_1 \in \{-1, -0.75, -0.5, -0.25, 0, 0.25, 0.5, 0.75, 1\}, \phi_x \in \{45°, 50°, 55°, 60°, 65°, 70°, 75°, 80°, 85°, 90°\}$, and $U_g \in [-10, 10]$ in steps of $\Delta U_g = 0.01$. Positive values of U_g are included in our investigation, because we consider $W_1 < 0$ and, hence, an attractor may possibly exist due to a balance between the fluid entertainment from the vertical wall and the gravitational settling. However, as demonstrated in the following, there are no attractors for $U_g > 0$ in $(\delta_x, \delta_z) \in [0.1, 1] \times [0.1, 1]$. To satisfy the condition $|\boldsymbol{x}| \ll L/a_p$ the particle motion is considered near the corner edge such that the distances δ_x and δ_z of the particle's surface from the two walls are restricted to $\delta_x = x_p - 1 \in [0, 1]$ and $\delta_z = z_p - 1 \in [0, 1]$. Due to the validity limits of the fit functions provided by Romanò *et al.* (2020*a*) our results are strictly valid only for particles at a distance $\delta \geq 0.1$ from the wall. Therefore, conclusions will be drawn only for $(\delta_x, \delta_z) \in [0.1, 1] \times [0.1, 1]$. We expect, however, the results can well be extended for practical purposes beyond the strict validity limits of the fit, because the fit includes the classical lubrication asymptotics, valid for either $\delta_x \to 0$ or $\delta_z \to 0$ (Romanò *et al.* 2020*a*).

Typical phase portraits for $(W_1, U_g) = (0, -1)$ (gravity force acting in the negative z direction) and $\phi_x = 90°, 75°, 65°$, and $60°$ are depicted in figure 3. Particle trajectories in the particle phase space are shown by thin solid lines with arrows indicating the flux vector (U, W). Obviously, the particle is attracted to a sink $\boldsymbol{x}_p^*$ for the current parameters. The white bullet marks the spiral sink which is a stagnation point of the particle flow field in the (x, z) subspace. The thick solid lines indicate the zeros of the z- and x-components of the velocity field of the particle, i.e. $W = 0$ (light blue) and $U = 0$ (light green).
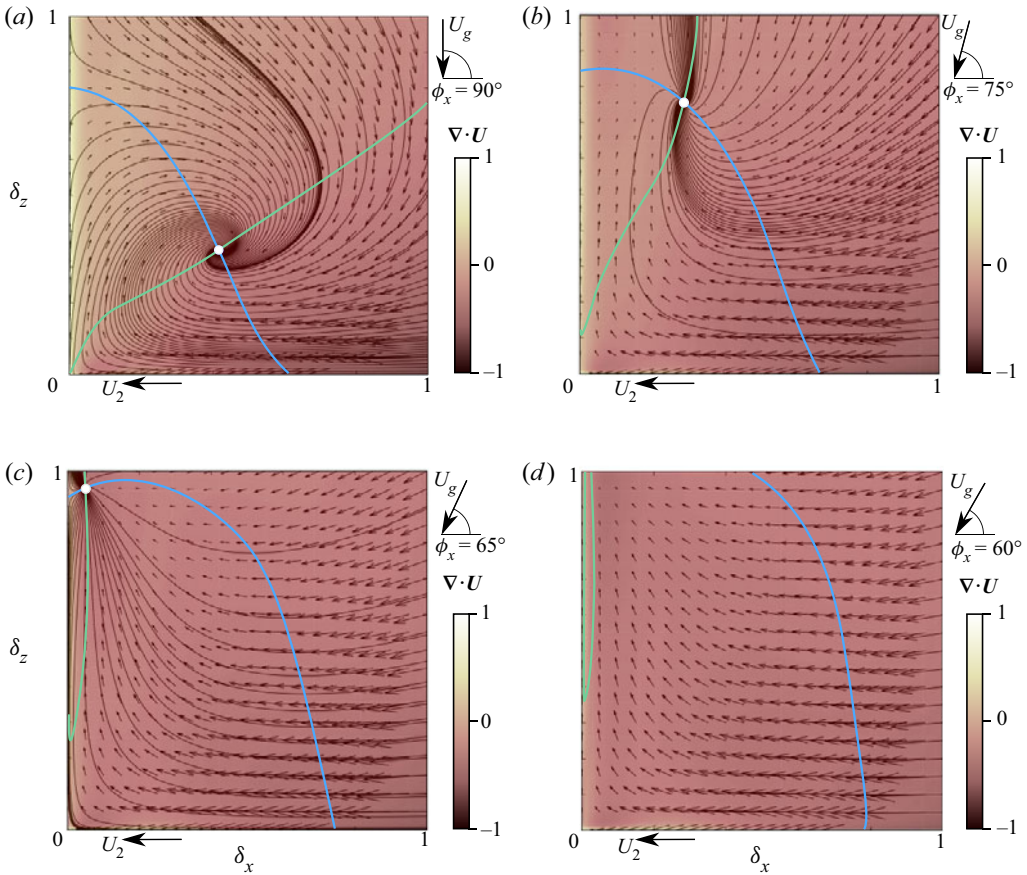
Figure 3. Phase portraits of $\dot{\boldsymbol{x}}_p = \boldsymbol{U}$ in the (δ_x, δ_z) plane for $(W_1, U_g) = (0, -1)$ and (a) $\phi_x = 90°$, (b) 75°, (c) 65°, (d) 60° with spiral sinks $\boldsymbol{x}_p^*$ indicated by the white bullets. The arrows show the particle velocity field $\boldsymbol{U}$ and the solid black lines are the particle trajectories spiralling into the attractor. Since the phase portrait is depicted in terms of δ_x and δ_z, the walls are located at $\delta_x = -1$ and $\delta_z = -1$. The thick solid lines indicate $U = 0$ (light green) and $W = 0$ (light blue). The colour maps represents the local expansion/contraction rate $\boldsymbol{\nabla} \cdot \boldsymbol{U}$.

For $\phi_x = 90°$, the stationary point is located at $(\delta_x, \delta_z)^* = (0.418, 0.346)$, detached from the walls. Apart from this spiral sink, a saddle point attracting in z and repelling in x is identified at $(\delta_x, \delta_z)^* = (0, 0.794)$. However, due to the aforementioned limitations ($\delta_x > 0.1$ and $\delta_z > 0.1$) we only characterise stationary points located sufficiently far from the walls. For $\phi_x = 75°$, the sink is located at $(\delta_x, \delta_z)^* = (0.289, 0.755)$, for $\phi_x = 65°$ at $(\delta_x, \delta_z)^* = (0.046, 0.958)$, while no attractor has been found for $\phi_x = 60°$ within the domain $(\delta_x, \delta_z) \in [0.1, 1] \times [0.1, 1]$. From the colour maps provided in figure 3, the flux field has a negative divergence $\boldsymbol{\nabla} \cdot \boldsymbol{U} < 0$, except, possibly, near the stationary vertical wall, and the particle phase space is contracting.

4.2. *Local flow and stress distribution*

As an example, we computed the local flow near a sphere for $U_2 = -1$, $\phi_x = 90°$, $U_g = -1$ and $W_1 = 0$ corresponding to figure 3(a), using the code of Romanò *et al.* (2020a). Figure 4 shows the flow field in the vicinity of the sphere in the symmetry plane $y = 0$
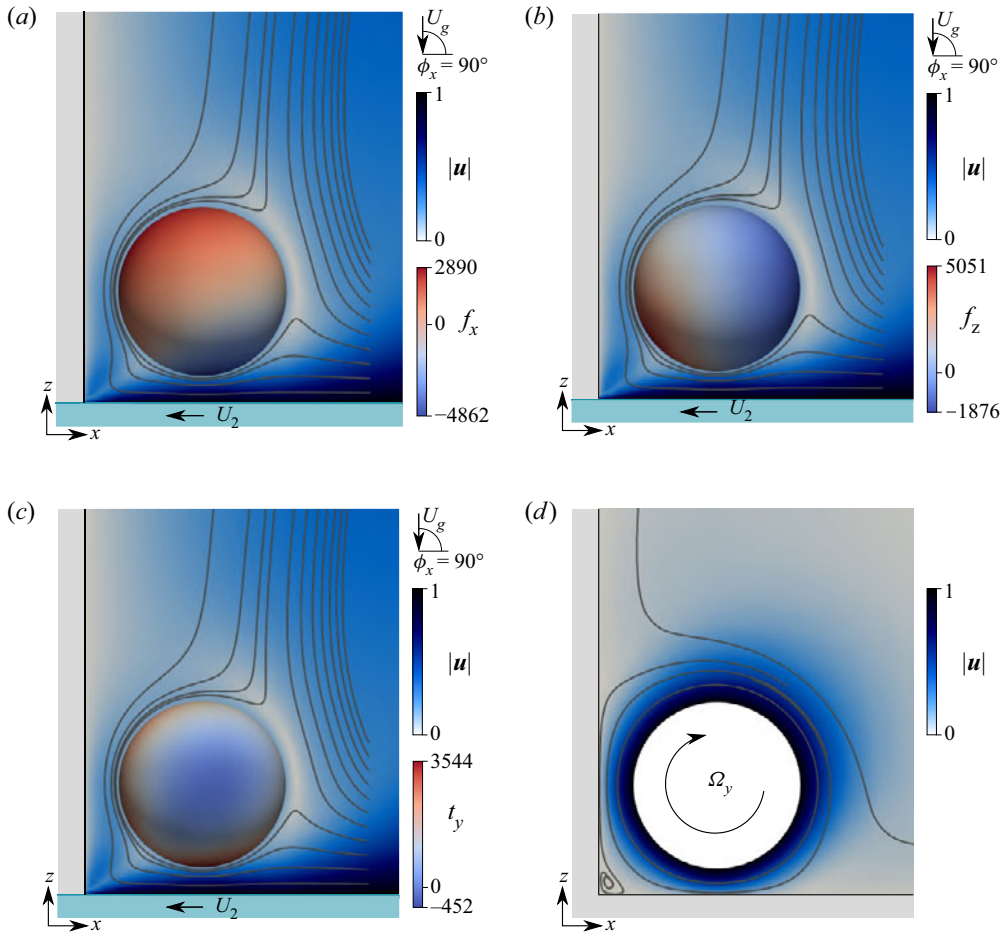
Figure 4. Flow near a sphere in its fixed point $(\delta_x, \delta_z) = (0.418, 0.346)$ for $(W_2, U_g, \phi_x) = (0, -1, 90°)$. Outside of the sphere the velocity magnitude $|\boldsymbol{u}|$ (blue shading) and streamlines (dark grey) are shown in the plane $y = $ const. through the sphere's centre $(a–c)$. Inside the circle delineating the sphere the local stresses f_x in the x direction (a), f_z in the z direction (b) and torque t_y in the y direction (c) on the surface of the sphere are shown, projected to the plane $y = $ const. Streamlines and absolute value of the velocity $|\boldsymbol{u}|$ are shown in panel (d) for the case when the centre of the sphere is fixed and it rotates in the y direction with the same angular velocity Ω_y as in panels $(a–c)$ but with all walls being stationary.

after it has been attracted to its fixed point. While $U = W = 0$, the particle rotates with $\Omega_y = 0.15$. Therefore, the total flow is a linear combination of problem II (particle rotation in the y direction) and problem VIb (bottom wall motion in the x direction).

In addition to the flow field, figure 4(a) displays the local stress f_x in the x direction evaluated on the surface of the sphere. The local stress is scaled consistently with the creeping-flow scaling, hence f_x is non-dimensionalised with $\rho_f \nu^2 / a_p^2$. The flow in the negative x direction leads to a net force component F_x (integral of surface stresses f_x) in the negative x direction, while the flow passing behind the sphere generates a counter-balancing force, resulting in an equilibrium in the x direction. From figure 4(b) the surface stresses f_z in the positive z direction, non-dimensionalised with $\rho_f \nu^2 / a_p^2$, dominate. They are, however, balanced by the gravitational force in the negative z direction. It is

927 A41-10

apparent that the stress distribution causes a torque (the local contribution to the torque in the y direction t_y, non-dimensionalised with $\rho_f \nu^2 / a_p^3$, is shown on the particle surface in figure 4c) which leads to a clockwise rotation of the sphere. The absolute value of the flow velocity near the right-hand side of the sphere is particularly weak, because the flow due to the rotation of the sphere locally balances the flow due to the wall motion.

As the sphere is rotating and not translating in the fixed point, it is interesting to compare the situation with problem II in which all walls are at rest, but the sphere is assumed to rotate with the same angular velocity as a sphere caught in the fixed point (figure 4a–c). The corresponding flow field is shown in figure 4(d). Apart from the modification of the exterior flow due to the absence of the entrainment effect of the wall motion, we find a small counter-rotating vortex located at the corner edge. This resembles a localised three-dimensional version of a two-dimensional Moffatt eddy (Moffatt 1964) and is, in fact, a three-dimensional saddle focus, similar to what is found in a three-dimensional lid-driven cavity flow (see e.g. figure 6c in Romanò, Türkbay & Kuhlmann (2020b)). Obviously, the small counter-rotating vortex in figure 4(d) does not arise in the case of a sphere in its fixed point when the wall moves towards the edge (figure 4a–c), because the velocity a fixed sphere rotating with the same angular velocity induces at the periphery of the corner eddy is much smaller than the velocity induced by the moving wall at the same location.

4.3. *Dependence of the attractor location on the parameters*

The location $(\delta_x, \delta_z)^*$ of the spiral sink is shown in figure 5 as a function of the settling velocity U_g for different vertical wall velocities $W_1 = 0.25, 0, -0.25, -0.5, -0.75$ and -1. The dependence on the angle ϕ_x is indicated by colour. No attractors/repellers are found for $W_1 = 0.5$, $W_1 = 0.75$ and $W_1 = 1$ in the range $\phi_x \in [45°, 90°]$ for $(\delta_x, \delta_z) \in [0.1, 1] \times [0.1, 1]$. The stationary point has been obtained by numerically searching for the stagnation points of the two-dimensional particle velocity field (U, W) in the range $1 \geq \delta_x \geq 0.02$ and $1 \geq \delta_z \geq 0.02$ by integrating $\dot{x}_p$ forward and backward in time with initial conditions covering the whole domain. The attractor/repeller x_p^* is identified by the condition $|\dot{x}_p| < 10^{-4}$. Within the neighbourhood of $\dot{x}_p = 0$, such that $|\dot{x}_p| < 10^{-4}$, the fixed point is found by considering a structured grid with $\Delta \delta_x = \Delta \delta_z = 10^{-3}$ and identifying $\min_x(|\dot{x}_p|)$. The tolerance of $\Delta \delta_x$ and $\Delta \delta_z$ for x_p^* is of the order of accuracy of the fit functions provided by Romanò *et al.* (2020a). For the present normalisation $U_2 = -1$ the attractor always arises as a spiral sink $(\nabla \cdot U|_{x_p} < 0)$, whereas for $U_2 = 1$, with the signs of W_1 and U_g reversed, the critical point becomes a spiral source $(\nabla \cdot U|_{x_p} > 0)$.

Within the range of parameters considered, the free attractor near the edge at $(x, z) = (0, 0)$ is always found for a heavy particle $(U_g < 0)$ if the magnitude of the settling velocity $|U_g| = O(1)$ is not too large. The range of existence is always found to be confined to the interval $U_g \in [-2.2, -0.7]$ (note the ranges in figure 5). For $W_1 = 0$ the attractor results from a balance between the gravitational settling at an angle ϕ_x from the horizontal wall (wall 2) and the forces and torques exerted by the fluid on the particle owing to the finite size of the particle and the fluid entrainment due to the sliding wall $(U_2 = -1)$. In particular, the only fundamental problems contributing to the particle dynamics in the (x, z) subspace are problems II, IIIa, IIIb, VIb and VII (see (3.3a)). Decreasing the angle ϕ_x from 90° to 45° reduces the z and increases the x component of the gravity force opposing the viscous forces that repel the particle from the walls. As a result the location of the line attractor moves away from wall 2 and towards wall 1. When the absolute value of the settling velocity decreases, the particle attractor moves away from the corner, because
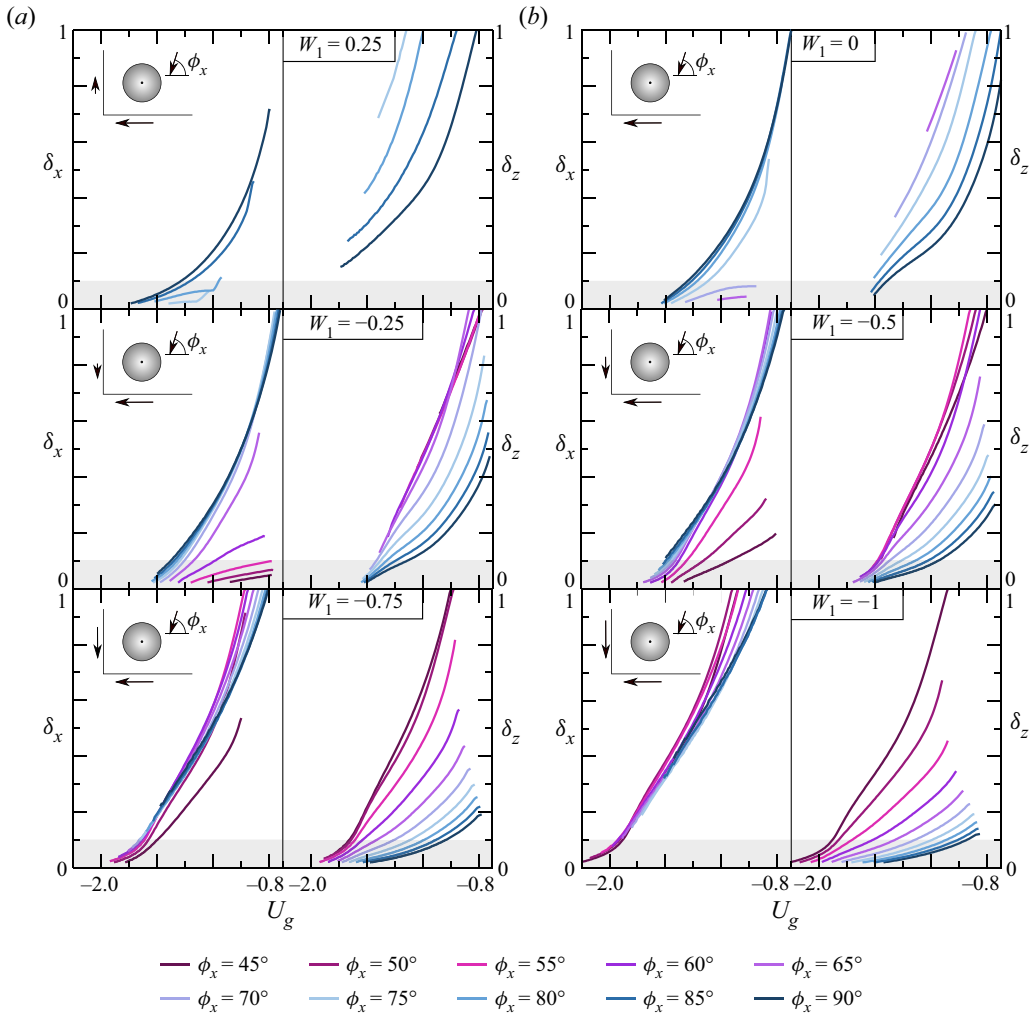
Figure 5. Coordinates δ_x^* (*a*) and δ_z^* (*b*) of the locus of the spiral sink as functions of the settling velocity U_g and W_1 (indicated at the top left of the right panel of each subfigure). Different angles ϕ_x are indicated by colour. The grey strip at the bottom indicates the region outside of the strict domain of validity of the fit functions of Romanò *et al.* (2020*a*).

the equilibrium of forces on the particle is found for smaller fluid flow velocities. This behaviour can also be recognised from figure 6 which shows projections of the path upon a variation of U_g of the attractor x_p^* in the particle phase space (δ_x, δ_z) for constant ϕ_x and W_1 as indicated in the figure. No attractors/repellers are found for $W_1 = 0.5$, $W_1 = 0.75$ and $W_1 = 1$ in the range $\phi_x \in [45°, 90°]$ for $[0.1, 0.1] < [\delta_x, \delta_z] < [1, 1]$.

When the wall 1 slides at a constant velocity W_1, problem VIa also contributes to the particle attractor (see (3.3*a*)), which results from the balance between the settling effect and the entrainment by the two walls. Increasing W_1 from zero, the forces and torques exerted by the fluid due to the entrainment from wall 1 have a net opposing effect to the gravitational settling and the locus of the attractor moves closer to wall 1. On the other hand, decreasing W_1 from zero, the attractor location moves closer to wall 2. This can be seen from the different panels in figure 6. From this figure it also appears as if the free

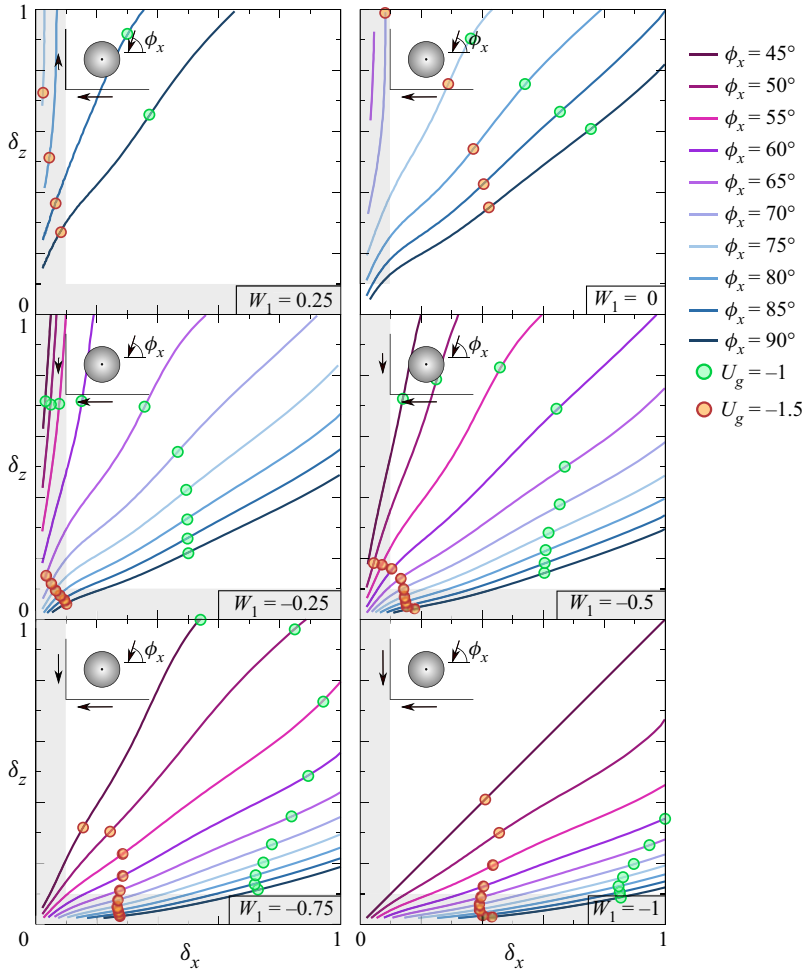Figure 6. Location of the attractor $x_p^* = (1 + \delta_x^*, 1 + \delta_z^*)$ for different angles ϕ_x (indicated by colour) and wall velocities W_1 (indicated at the bottom right of each subfigure). As the settling velocity U_g is increased, the attractor x_p^* travels towards the apex (lower left) along the curves shown. The green and orange markers denote the attractor location for $U_g = -1$ and $U_g = -1.5$, respectively. The grey strips at the bottom and on the left indicate the region outside of the strict domain of validity of the fit functions of Romanò *et al.* (2020*a*).

particle attractors originate, for large absolute values of the (negative) settling velocity, from wall 2 for $W_1 \gtrsim -0.5$, whereas they originate from wall 1 for $W_1 \lesssim -0.5$. For $W_1 > 0.25$ no detached particle attractor is found in $(\delta_x, \delta_z) \in [0.1, 1] \times [0.1, 1]$, because the entrainment due to wall 1 is too strong to allow for a free equilibrium near the corner. Similarly, if the angle of the gravitational acceleration is too small, i.e. $\phi_x < 75°$ for $W_1 = 0.25$, the component of the gravity force opposing the particle uplift is not strong enough to allow for a free equilibrium near the corner. The non-monotonic variation of the location of the attractor as a function of the governing parameters, like for example δ_z, results from a delicate balance between opposing individual forces. Even though the Cartesian components of the individual forces to the total force may depend monotonically on a parameter, the Cartesian components of the resulting total force, hence the attractor location, can vary non-monotonically.
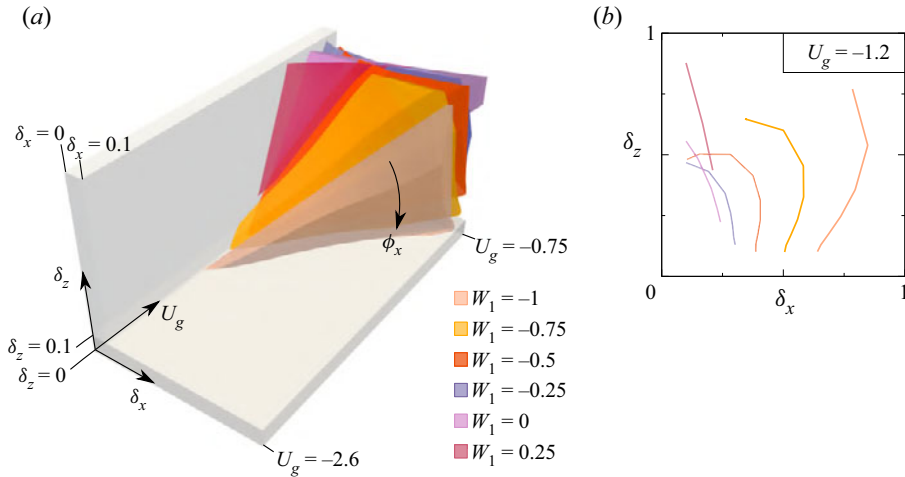
Figure 7. (*a*) Three-dimensional reconstruction of the location of the attractor in form of hypersurfaces reconstructed for constant W_1. (*b*) Cross-section of the hypersurfaces at $U_g = -1.2$.

To illustrate the region in which the particle attractors arise, figure 7(*a*) shows a three-dimensional view of the subspace spanned by δ_x, δ_z and U_g. For constant W_1 the attractor then lies on a surface which is characterised by U_g and ϕ_x. In figure 7(*a*) these surfaces are distinguished by colour (parameterising W_1), while the dependence of the locus of the attractor on ϕ_x is not explicitly given; merely, the direction of increasing ϕ_x is indicated. The nested structure of these hypersurfaces is demonstrated in figure 7(*b*) which depicts a cross-section at $U_g = -1.2$ with the same colour coding as in figure 7(*a*).

4.4. *Application to a non-Stokesian flow in a finite domain*

The results obtained for the behaviour of a particle in Stokes flow near a semi-infinite right corner can be applied to improve the one-way coupled particle motion in a closed flow at a finite Reynolds number. This is demonstrated by considering the particle motion in a two-dimensional incompressible flow in a two-sided lid-driven square cavity (Albensoeder, Kuhlmann & Rath 2001) as sketched in figure 8. The approach is demonstrated using a variant of the Maxey–Riley equation for the particle motion in the bulk. Since the Maxey–Riley approximation breaks down near the walls, we introduce extra forces in the Maxey–Riley equation such that the correct particle dynamics is recovered as a wall or a singular corner is approached. Similar approaches have widely been used in the literature to complement the Maxey–Riley equation by dedicated particle–boundary models (Kharlamov, Chára & Vlasák 2008; Yang 2010; Agarwal, Rallabandi & Hilgenfeldt 2018; Davies *et al.* 2018; Romanò 2019; Romanò *et al.* 2019*a*; Agarwal *et al.* 2021; Magnaudet & Abbas 2021).

In the present approach the extra forces near the boundary are based on the fit provided by Romanò *et al.* (2020*a*) which takes into account the exact solutions and the asymptotic lubrication theory for a particle moving towards/away from a wall. Therefore, the correction to the Maxey–Riley equation is expected to be valid not only in the strict corner region within which the fit was made (red square in figure 8), but also farther away from the corner when the particle approaches one of the two walls much closer than the other (further details can be found in Romanò *et al.* (2020*a*)). By this approach weak inertial effects on the corner attractor can be identified.
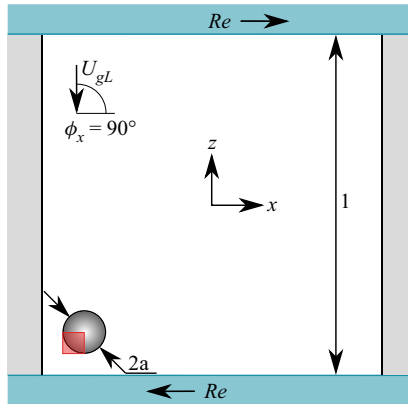
927 A41-14

Figure 8. Sketch of a two-dimensional square cavity within which a global flow is driven by an antisymmetric wall motion (arrows). The motion of a particle is considered when its centroid is located inside the red square which outlines the region of validity of the force and torque coefficients provided by Romanò *et al.* (2020*a*). In units of the non-dimensional particle radius $a = a_p/L$ the square has a size $a \times a$ and a distance a from both walls, where L is the cavity height. The particle is shown for the case when its centroid is located at its maximum distance, admitted by Romanò *et al.* (2020*a*), from the lower left corner. U_{gL} is the settling velocity based on the length L instead of a_p.

The steady flow induced by the moving walls of the cavity must satisfy the Navier–Stokes equations

$$(\boldsymbol{u} \cdot \boldsymbol{\nabla}) \, \boldsymbol{u} = -\boldsymbol{\nabla} p + \Delta \boldsymbol{u}, \tag{4.1a}$$

$$\boldsymbol{\nabla} \cdot \boldsymbol{u} = 0, \tag{4.1b}$$

where we used a viscous scaling, as in table 1, but with the relevant length scale given by the width L of the square cavity instead of the particle radius a_p. In this scaling the velocity field $\boldsymbol{u}$ must satisfy the boundary conditions

$$\boldsymbol{u}(z \pm 1/2) = (\pm Re, 0)^{\mathrm{T}}, \tag{4.2}$$

$$\boldsymbol{u}(x \pm 1/2) = \boldsymbol{0}, \tag{4.3}$$

where the Reynolds number of the flow is defined as

$$Re = \frac{U_L L}{\nu}, \tag{4.4}$$

with U_L the magnitude of the lid velocity. The following analysis will be restricted to moderate Reynolds numbers ($Re \leq 100$), for which the flow is steady and two-dimensional (Albensoeder & Kuhlmann 2003).

In the limit $Re \to 0$ and with the acceleration of gravity $\boldsymbol{g} = (0, -g)^{\mathrm{T}}$, a small particle would not find a stationary point near the corners $(x, z) = (0.5, \pm 0.5)$ (on the right-hand side in figure 8). From the analysis reported in § 4.1, an attractor for the particle motion is expected near the corner $(x, z) = (-0.5, -0.5)$, while near $(x, z) = (-0.5, 0.5)$ a repeller is expected.

Here we focus on the particle motion near $(x, z) = (-0.5, -0.5)$ and its approach to the attractor when the Reynolds number is $Re = O(1)$. For a small particle Reynolds number $\widehat{Re}_p \ll 1$ and if the time scale of the particle τ_p is much smaller than that of the fluid, i.e. if $\tau_p/\tau_f = (a_p^2/\nu)(U_L/L) \ll 1$, the particle motion in the bulk can be modelled

by one-way coupling. In this approach the flow field is independent of the presence of the particle and can be computed beforehand. Here we use a simplified version of the Maxey–Riley equation (Maxey & Riley 1983) as in (Babiano *et al.* 2000)

$$\ddot{x} = \frac{1}{\varrho + 1/2} \left[-\frac{\varrho}{St} (\dot{x} - u) + \frac{3}{2} \frac{Du}{Dt} - (\varrho - 1) \frac{e_z}{Fr_L^2} \right], \qquad (4.5)$$

where the Stokes and the Froude numbers based on the length of the side walls are defined by

$$St = \frac{2}{9} \varrho a^2, \quad Fr_L^2 = \frac{\nu^2}{gL^3}, \qquad (4.6a,b)$$

and $a = a_p/L$ is the relative particle radius.

The form of the Stokes drag in (4.5) is not correct when the particle moves near the boundaries. In order to incorporate the correct viscous effects on the particle motion near the corner $(x, z) = (-0.5, -0.5)$, the Stokes part u_S of the total velocity field u is separated by writing

$$u = u_S + u', \qquad (4.7)$$

where u' is the inertial remainder. The term $(\dot{x} - u_S)$ in the drag force due to the Stokes part u_S of the flow, which is contained in $(\dot{x} - u)$ of (4.5), is now replaced by the numerical approximation of the correct drag forces acting on the sphere obtained by Romanò *et al.* (2020*a*) and used in the previous sections. Taking into account the different scalings used here and in § 3 we obtain

$$\ddot{x} = \frac{1}{\varrho + 1/2} \left[\frac{\varrho}{St} \left(\dot{x} \cdot e_x F^{IIIa} + \dot{x} \cdot e_z F^{IIIb} + Re F^{VIb} + a F^{IIa} \frac{\omega}{2} + u' \right) \right.$$
$$\left. + \frac{3}{2} \frac{Du'}{Dt} - \frac{\varrho - 1}{Fr_L^2} e_z \right]. \qquad (4.8)$$

By replacing the Stokes part of the drag force, the rotation rate Ω_y of the particle enters (4.8). Because this quantity is not available through the Maxey–Riley equation (4.5), it is modelled here by $\omega/2$, with $\omega = (\nabla \times u) \cdot e_y$ the vorticity of the total flow.

Note (4.8) is valid only within the region (shown as a red square in figure 8) for which the correlations of Romanò *et al.* (2020*a*) have been obtained and within which the particle attractor is located in the Stokes flow limit $u' \to 0$. It is expected that the attractor can be found in this region also for weakly inertial flow ($u' \neq 0$) in the framework of approximation (4.8). For all simulations carried out, the local particle Reynolds number is moderate with $\widehat{Re}_p \lesssim 1$ (see figure 9*b* below), as required by the Maxey–Riley equation.

To be able to simulate particle trajectories using the corner-improved model (4.8), first the total flow field u is computed in the whole domain $(x, z) \in [-1/2, 1/2] \times [-1/2, 1/2]$ for $Re \in [10^{-4}, 10^{-2}, 1, 25, 50, 75, 100]$, using the finite element library FEniCS (Alnæs *et al.* 2015) and a 200×200 basic mesh which is further refined by reducing the grid spacing by a factor of two at each of the distances 0.05, 0.01 and 0.005 from all walls. The velocity and pressure are discretised using Taylor–Hood elements in which the velocity is approximated by piecewise quadratic polynomials, while the pressure is represented by piecewise linear polynomials. Using the Stokes flow solution (2.3) valid near the corner $(x, z) = (-1/2, -1/2)$ the inertial part of the flow u' near this corner is obtained from (4.7).
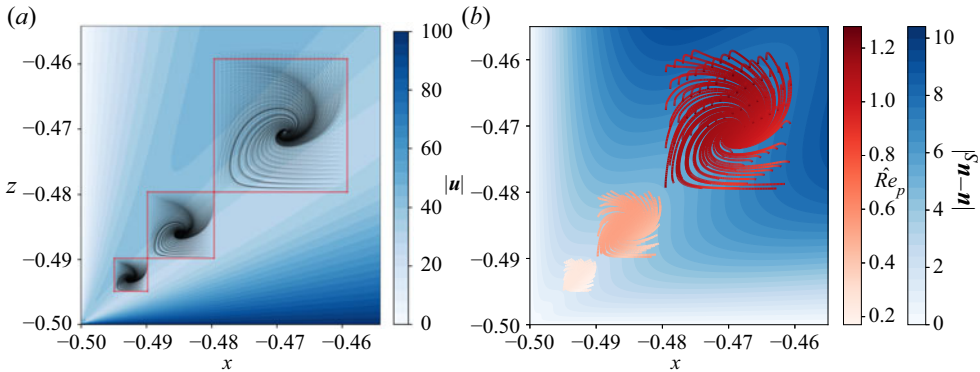
Figure 9. (*a*) Particle trajectories converging towards the corner attractor near $(x, z) = (-0.5, -0.5)$, and initialised velocity matched on a 31×31 tensor grid defined with the bounds $(\delta_x, \delta_z) \in [0.025, 0.975] \times [0.025, 0.975]$ for $Re = 100$ and $a = 0.005$, 0.01 and 0.02 (solid lines). The colour map corresponds to the non-dimensional flow velocity magnitude. (*b*) Blue shades indicate the magnitude of the deviation from the Stokes corner flow, while red shading indicates the local particle Reynolds $\widehat{Re}_p$ number computed along every ninth particle trajectory as a function of time.

To probe the attractor, particles were initiated velocity matched to the flow on a regular 11×11 grid within $[-1/2 + 1.025a, -1/2 + 1.975a] \times [-1/2 + 1.025a, -1/2 + 1.975a]$, inside the red square in figure 8, and (4.8) was integrated in time using the fourth-order 3/8-rule Runge–Kutta method for different particle radii $a \in [0.02, 0.01, 0.005]$. The relative density is kept constant at $\varrho = 1.01$.

Figure 9(*a*) shows three sets of particle trajectories (lines) for $a = 0.005$, 0.01 and 0.02, respectively, together with the velocity magnitude of the flow. For a reduced set of trajectories shown in figure 9(*b*), the saturation of the red colour indicates the local particle Reynolds number $\widehat{Re}_p = |\tilde{U} + \tilde{\Omega} \times (\tilde{x}_s - \tilde{x}_p) - \tilde{u}|a_p/\nu$ along the particle trajectories together with the magnitude of the inertial remainder (blue).

After a short transient all particles were found to be attracted to the same unique attractor, depending on the particle size and on the Reynolds number Re. In the case of $a = 0.02$, owing to the larger Stokes number, some particles initialised in the upper part of the seeding region, shown in red in figure 8 and 9(*a*), briefly leave the region of validity of the model (4.8). To treat the particle motion outside of the strict domain of validity (red square in figure 8) the correlations for F^{IIIa}, F^{IIIb}, F^{VIb} and F^{IIa} of Romanò *et al.* (2020*a*) have been extrapolated slightly beyond the original domain of validity by employing the fit also for $\delta_z > 1$. However, very similar results are obtained when abruptly switching from the model of Romanò *et al.* (2020*a*) to a particle–boundary interaction which only takes into account forces from the plane stationary and moving walls (Jeffery 1915; Brenner 1961; Chaoui & Feuillebois 2003), not taking into account the entrainment effect of the corner flow. In all cases, however, the fixed point is practically unaffected by the exterior model and the phase portraits near the fixed point are qualitatively equivalent to the one shown in figure 3(*a*). Therefore, the attraction dynamics predicted under the creeping-flow approximation is robust with respect to the addition of small inertial effects and to the particle–boundary interaction model used outside of the red region. Because all particles of the same kind initialised in one of the red regions are attracted to the same unique attractor, the prediction of the Stokesian attractor can be safely generalised to realisable systems such as the present cavity flow.
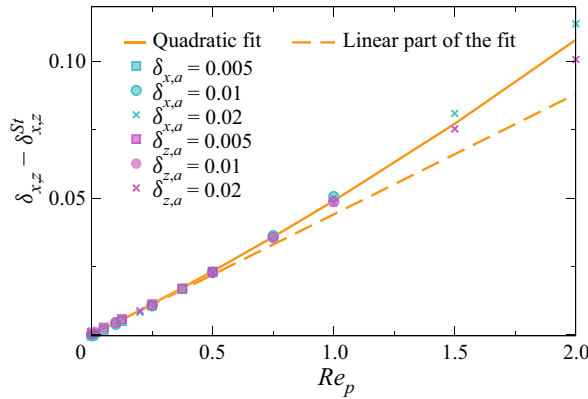
Figure 10. Displacements in the x direction (turquoise) and in the z direction (violet) of the attractor near the corner $(x, z) = (-1/2, -1/2)$ as functions of the global particle Reynolds number and for different particle sizes (symbols). The full line is the quadratic fit (4.9) whose linear part is indicated by the dashed line.

The location of the attractor is shown in figure 10 in terms of the displacement $(\delta_{x,z} - \delta_{x,z}^{St})$ relative to the attractor in Stokes flow $(\delta_x^{St}, \delta_z^{St}) = (0.418, 0.346)$ (see figure 4(a)). The displacements in the x and z direction for different particles sizes and flow Reynolds numbers Re nearly collapse on a single curve satisfying

$$\delta_{x,z} - \delta_{x,z}^{St} \approx 0.04408 \, Re_p + 0.00495 \, Re_p^2, \tag{4.9}$$

which asymptotes to $(\delta_{x,z} - \delta_{x,z}^{St}) \approx 0.044 \, Re_p$ for $Re_p \to 0$ (dashed line in figure 10), where Re_p denotes the global particle Reynolds number $Re_p = aRe$. The collapse of all data to the almost linear curve (4.9) indicates that the relevant parameter measuring the displacement is indeed the global particle Reynolds number Re_p (here $Re_p \leq 2$) and that the position of the attractor is shifted away from the corner under an angle of $\approx 45°$ with respect to the x axis.

In creeping cavity flow a particle repeller is located near $(x, z) = (-1/2, 1/2)$ (near the upper left-hand corner in figure 8), symmetrically placed with respect to the horizontal cavity midplane $(z = 0)$ to the attractor in the lower left-hand corner. Upon an increase of the particle Reynolds numbers, this symmetry is broken: the bottom left attractor moves away from the corner, whereas the top left repeller moves towards the corner. Preliminary computations indicate the same linear asymptotic scaling of the displacement of the repeller for small particle Reynolds number, albeit with a different sign.

The model (4.8) based on the Maxey–Riley equation predicts the existence and location of the corner attractor also for inertial flow. Based on the results obtained it is expected that the attractor is robust and, for moderate Reynolds numbers, will neither be destroyed by higher-order inertial effects not included in (4.8) nor by the nonlinear interaction of the flow with the particle. Therefore, the attractor should also be observable in experiments. A thorough experimental proof, however, is pending.

5. Discussion and conclusion

The Stokesian dynamics of a freely translating and rotating spherical particle near a right dihedral corner was studied for the case when both walls are sliding tangentially to their planes and the gravitational force acts on the particle in an arbitrary direction. By making use of the quasi-steady approach valid for creeping flows, the particle's translational and

rotational velocities were expressed by the forces and torques acting on the particle. Based on the fit functions for the forces and torques provided by Romanò *et al.* (2020*a*) for the same set-up, the translational and rotational velocities of the particle could be expressed explicitly. This allowed for an extensive parametric study to determine particle trajectories for more than 180 000 configurations.

We find a non-trivial particle attractor in the (x, z) plane in the form of a spiral sink detached from the walls for $U_2 = -1$, $W_2 \in [-1, 0.25]$, $U_g \in [-2.2, -0.7]$ and $\phi_x \in [45°, 90°]$. The attracting line in the flow field U of the particle results from a stable balance between lift forces on the particle due to the fluid entrained by the sliding walls and the gravitational force directed towards the walls. Far away from the corner, the Stokesian lift decays (in creeping flow a particle near a plane does not experience any lift force) and the particle settles on one of the two walls, depending on U_g, ϕ_x and its initial location. Owing to the symmetry of the Stokesian flow, corresponding repellers are found by inverting the sign of W_1, U_2 and U_g. As the flow field for dihedral corners (without particles) does not experience abrupt changes of its topology upon a smooth variation of the dihedral angle, we expect our results are robust with respect to small deviations of the corner angle from the 90° considered in this study. This expectation is supported by the results of Dauparas & Lauga (2018), who found that the forces and torques on a particle far from the corner vary smoothly with the dihedral angle.

The particle attractor/repeller cannot be inferred from the velocity field u of the fluid alone. The velocity of the particle U is strongly influenced by gravity, the strength of which is measured by the settling velocity U_g, whereas the fluid flow field u is independent of the gravitational acceleration for isothermal incompressible flows.

Based on the definition of U_g, i.e. $U_g = 2(1 - \varrho)ga^3/9\nu^2$, the range $U_g \in [-2.2, -0.7]$ for heavy particles can be relevant for small particles ($a \in [10^{-4}, 10^{-3}]$ m) in liquids ($\nu \sim \in [10^{-6}, 10^{-3}]$ m^2 s^{-1}), for which several combinations of a and ν can be found such that $a^3/\nu^2 = O(1)$ s^2 m^{-1} and $(1 - \varrho) \approx O(1)$. As discussed further below, cavity and junction flows of characteristic lengths up to a few hundreds micrometres represent optimal set-ups for observing corner particle trapping of micron-sized particles.

Several examples of non-trivial finite-size particle attractors in non-chaotic Stokes flows have been reported in the literature. For instance, Sauma-Pérez *et al.* (2018) studied the emergence of a limit cycle for a particle in a rotating drum. For asymptotically small particle Reynolds numbers the theory predicts equilibrium positions resulting from the balance between gravitational, history, inertial forces and Stokes drag. However, owing to the finite-size of the particle, the particle trajectory undergoes a Hopf bifurcation which leads to a stable limit cycle whose size depends on the particle Reynolds number. This non-trivial attractor relates to the finite-size effects in the bulk. Other non-trivial limit cycles are reported for cavity flows (either shear- or lid-driven), where the limit cycle results from a balance between particle inertia and particle–boundary interaction due to the finite particle size. Examples of such limit cycles are reported in Romanò & Kuhlmann (2016), Romanò *et al.* (2017) and Romanò & Kuhlmann (2017). Similar non-trivial limit cycles have recently been reported by Romanò (2021), where inertial and Coriolis forces are balanced by particle–boundary interactions leading to particle limit cycles in a confined periodically rotating flow. The present study does complement the current literature by demonstrating that particle attractors/repellers exist in two-sided lid-driven cavities near two of the four corners as a result of a balance between gravitational settling and flow entrainment due to the finite particle size.

Apart from closed cavity flows as the one presented in § 4.4, similar corner attractors are expected for microfluidic set-ups, such as, for example, a T-junction used as a flow splitter.

In this case, the midplane would be equivalent to a free surface playing the role of a sliding wall, with the difference that the velocity would increase radially from the stagnation line rather than being constant along the driving boundary. In such a set-up, the corner attractor can be observed near the wall at the midplane of symmetry (see figure 3 of Chan, Haward & Shen (2018)). Another related set-up is a channel flow past an open microcavity (groove). The flow inside such cavity is driven by the shear layer formed between the channel flow and the recirculating flow inside the cavity. A particle clustering corresponding to our corner attractor has been experimentally observed by Hur, Mach & Di Carlo (2011) right before the complete release of particles in the channel. Another example of particle clustering near a corner with a driving surface has been experimentally observed for D-junctions by Volpe *et al.* (2017).

We expect the particle attraction/repulsion mechanism unravelled by our study will have an impact on those microfluidic applications in which the flow can be considered Stokesian and is seeded with non-interacting density-mismatched particles. Our study suggests that the positioning of a particle in a free stationary point can be controlled near a singular corner by the orientation of the device with respect to the gravity vector and by the wall velocities. This provides a novel strategy for corner-cleaning applications in microfluidic devices, where the microscopic chips can easily be inclined. In fact, our parametric study shows no corner attractors are formed beyond specific inclination angles ϕ_x of the walls. Moreover, as the Stokesian flow considered admits repellers as counterpart of the attractors, conditions can be identified for which the corner flow admits a repeller such that particles cannot be attracted to the corner. Finally, based on our point-particle simulations, we demonstrated that the attractors/repellers predicted in a semi-infinite corner can be relevant for mildly inertial flows in realisable geometries such as driven cavities.

Declaration of interests. The authors report no conflict of interest.

Author ORCIDs.

Ⓓ Francesco Romanò https://orcid.org/0000-0002-9511-4718;

Ⓓ Pierre-Emmanuel des Boscs https://orcid.org/0000-0002-2656-1434;

Ⓓ Hendrik C. Kuhlmann https://orcid.org/0000-0003-1783-3255.

REFERENCES

AGARWAL, S., CHAN, F.K., GAZZOLA, M. & HILGENFELDT, S. 2021 An unrecognized force in inertial microfluidics. arXiv:2101.03322.

AGARWAL, S., RALLABANDI, B. & HILGENFELDT, S. 2018 Inertial forces for particle manipulation near oscillating interfaces. *Phys. Rev. Fluids* **3** (10), 104201.

ALBENSOEDER, S. & KUHLMANN, H.C. 2003 Stability balloon for the double-lid-driven cavity flow. *Phys. Fluids* **15** (8), 2453–2456.

ALBENSOEDER, S, KUHLMANN, H.C. & RATH, H.J. 2001 Multiplicity of steady two-dimensional flows in two-sided lid-driven cavities. *Theor. Comput. Fluid Dyn.* **14** (4), 223–241.

ALNÆS, M., BLECHTA, J., HAKE, J., JOHANSSON, A., KEHLET, B., LOGG, A., RICHARDSON, C., RING, J., ROGNES, M.E. & WELLS, G.N. 2015 The fenics project version 1.5. *Arch. Num. Soft.* **3** (100), 9–23.

BABIANO, A., CARTWRIGHT, J.H.E., PIRO, O. & PROVENZALE, A. 2000 Dynamics of a small neutrally buoyant sphere in a fluid and targeting in hamiltonian systems. *Phys. Rev. Lett.* **84** (25), 5764–5767.

BRENNER, H. 1961 The slow motion of a sphere through a viscous fluid towards a plane surface. *Chem. Engng Sci.* **16** (3–4), 242–251.

CHAN, S.T., HAWARD, S.J. & SHEN, A.Q. 2018 Microscopic investigation of vortex breakdown in a dividing t-junction flow. *Phys. Rev. Fluids* **3** (7), 072201.

CHAOUI, M. & FEUILLEBOIS, F. 2003 Creeping flow around a sphere in a shear flow close to a wall. *Q. J. Mech. Appl. Maths* **56** (3), 381–410.

COX, R.G. & MASON, S.G. 1971 Suspended particles in fluid flow through tubes. *Annu. Rev. Fluid Mech.* **3** (1), 291–316.

DAMIANO, E.R., LONG, D.S., EL-KHATIB, F.H. & STACE, T.M. 2004 On the motion of a sphere in a Stokes flow parallel to a Brinkman half-space. *J. Fluid Mech.* **500**, 75–101.

DAUPARAS, J. & LAUGA, E. 2018 Leading-order Stokes flows near a corner. *IMA J. Appl. Maths* **83** (4), 590–633.

DAVIES, H.S., DÉBARRE, D., EL AMRI, N., VERDIER, C., RICHTER, R.P. & BUREAU, L. 2018 Elastohydrodynamic lift at a soft wall. *Phys. Rev. Lett.* **120** (19), 198001.

DONOLATO, M., GOBBI, M., VAVASSORI, P., LEONE, M., CANTONI, M., METLUSHKO, V., ILIC, B., ZHANG, M., WANG, S.X. & BERTACCO, R. 2009 Nanosized corners for trapping and detecting magnetic nanoparticles. *Nanotechnology* **20** (38), 385501.

EDWARDS, D.A., HANES, J., CAPONETTI, G., HRKACH, J., BEN-JEBRIA, A., ESKEW, M.L., MINTZES, J., DEAVER, D., LOTAN, N. & LANGER, R. 1997 Large porous particles for pulmonary drug delivery. *Science* **276** (5320), 1868–1872.

FAXÉN, H. 1927 Die Geschwindigkeit zweier Kugeln, die unter Einwirkung der Schwere in einer zähen Flüssigkeit fallen. *Z. Angew. Math. Mech.* **7** (1), 79–80.

FEUILLEBOIS, F., GHALYA, N., SELLIER, A. & ELASMI, L. 2011 Motion of particles in a parabolic flow near a slip wall. In *AIP Conference Proceedings*, vol. 1404, pp. 340–351. American Institute of Physics.

GOLDMAN, A.J., COX, R.G. & BRENNER, H. 1967a Slow viscous motion of a sphere parallel to a plane wall: I. Motion through a quiescent fluid. *Chem. Engng Sci.* **22** (4), 637–651.

GOLDMAN, A.J., COX, R.G. & BRENNER, H. 1967b Slow viscous motion of a sphere parallel to a plane wall: II. Couette flow. *Chem. Engng Sci.* **22** (4), 653–660.

HOFMANN, E. & KUHLMANN, H.C. 2011 Particle accumulation on periodic orbits by repeated free surface collisions. *Phys. Fluids* **23**, 0721106.

HUR, S.C., MACH, A.J. & DI CARLO, D. 2011 High-throughput size-based rare cell enrichment using microscale vortices. *Biomicrofluidics* **5** (2), 022206.

JEFFERY, G.B. 1915 On the steady rotation of a solid of revolution in a viscous fluid. *Proc. Lond. Math. Soc.* **2** (1), 327–338.

KARIMI, A., YAZDI, S. & ARDEKANI, A.M. 2013 Hydrodynamic mechanisms of cell and particle trapping in microfluidics. *Biomicrofluidics* **7** (2), 021501.

KHARLAMOV, A.A., CHÁRA, Z. & VLASÁK, P. 2008 Hydraulic formulae for the added masses of an impermeable sphere moving near a plane wall. *J. Engng Maths* **62** (2), 161–172.

KUEHN, C., ROMANÒ, F. & KUHLMANN, H.C. 2018 Tracking particles in flows near invariant manifolds via balance functions. *Nonlinear Dyn.* **92** (3), 983–1000.

KUHLMANN, H.C., ROMANÒ, F., WU, H. & ALBENSOEDER, S. 2016 Particle-motion attractors due to particle-boundary interaction in incompressible steady three-dimensional flows. In *The 20th Australasian Fluid Mechanics Conference* (ed. G. Ivey, T. Zhou, N. Jones & S. Draper), p. 102, Paper no. 449. Australasian Fluid Mechanics Society.

LENSHOF, A. & LAURELL, T. 2010 Continuous separation of cells and particles in microfluidic systems. *Chem. Soc. Rev.* **39** (3), 1203–1217.

LORENTZ, H.A. 1907 Ein allgemeiner Satz, die Bewegung einer reibenden Flüssigkeit betreffend, nebst einigen Anwendungen desselben. *Abh. Theor. Phys.* **1**, 23–42.

MAGNAUDET, J. & ABBAS, M. 2021 Near-wall forces on a neutrally buoyant spherical particle in an axisymmetric stagnation-point flow. *J. Fluid Mech.* **914**, A18.

MAXEY, M.R. & RILEY, J.J. 1983 Equation of motion for a small rigid sphere in a nonuniform flow. *Phys. Fluids* **26**, 883–889.

MOFFATT, H.K. 1964 Viscous and resistive eddies near a sharp corner. *J. Fluid Mech.* **18** (1), 1–18.

MUKIN, R.V. & KUHLMANN, H.C. 2013 Topology of hydrothermal waves in liquid bridges and dissipative structures of transported particles. *Phys. Rev.* E **88**, 053016.

MULDOON, F.H. & KUHLMANN, H.C. 2013 Coherent particulate structures by boundary interaction of small particles in confined periodic flows. *Physica* D **253**, 40–65.

ORLISHAUSEN, M., BUTZHAMMER, L., SCHLOTBOHM, D., ZAPF, D. & KÖHLER, W. 2017 Particle accumulation and depletion in a microfluidic Marangoni flow. *Soft Matt.* **13** (39), 7053–7060.

PAPAVASSILIOU, D. & ALEXANDER, G.P. 2017 Exact solutions for hydrodynamic interactions of two squirming spheres. *J. Fluid Mech.* **813**, 618–646.

ROMANÒ, F. 2019 Reconstructing the fluid flow by tracking of large particles. *Phys. Rev. Fluids* **4** (10), 104301.

ROMANÒ, F. 2021 Particle coherent structures in confined oscillatory switching centrifugation. *Crystals* **11** (2), 183.

ROMANÒ, F., DES BOSCS, P.-E. & KUHLMANN, H.C. 2020a Forces and torques on a sphere moving near a dihedral corner in creeping flow. *Eur. J. Mech.* B/*Fluids* **84**, 110–121.

ROMANÒ, F. & KUHLMANN, H.C. 2016 Numerical investigation of the interaction of a finite-size particle with a tangentially moving boundary. *Intl J. Heat Fluid Flow* **62 Part A**, 75–82.

ROMANÒ, F. & KUHLMANN, H.C. 2017 Particle–boundary interaction in a shear-driven cavity flow. *Theor. Comput. Fluid Dyn.* **31**, 427–445.

ROMANÒ, F. & KUHLMANN, H.C. 2018 Finite-size Lagrangian coherent structures in thermocapillary liquid bridges. *Phys. Rev. Fluids* **3** (9), 094302.

ROMANÒ, F. & KUHLMANN, H.C. 2019 Finite-size coherent structures in thermocapillary liquid bridges: A review. *Intl J. Microgravity Sci. Appl.* **36**, 360201.

ROMANÒ, F., KUHLMANN, H.C., ISHIMURA, M. & UENO, I. 2017 Limit cycles for the motion of finite-size particles in axisymmetric thermocapillary flows in liquid bridges. *Phys. Fluids* **29** (9), 093303.

ROMANÒ, F., KUNCHI KANNAN, P. & KUHLMANN, H.C. 2019*a* Finite-size Lagrangian coherent structures in a two-sided lid-driven cavity. *Phys. Rev. Fluids* **4** (2), 024302.

ROMANÒ, F., TÜRKBAY, T. & KUHLMANN, H.C. 2020*b* Lagrangian chaos in steady three-dimensional lid-driven cavity flow. *Chaos* **30** (7), 073121.

ROMANÒ, F., WU, H. & KUHLMANN, H.C. 2019*b* A generic mechanism for finite-size coherent particle structures. *Intl J. Multiphase Flow* **111**, 42–52.

SAUMA-PÉREZ, T., JOHNSON, C.G., YANG, L. & MULLIN, T. 2018 An experimental study of the motion of a light sphere in a rotating viscous fluid. *J. Fluid Mech.* **847**, 119–133.

SCHWABE, D., HINTZ, P. & FRANK, S. 1996 New features of thermocapillary convection in floating zones revealed by tracer particle accumulation structures (PAS). *Microgravity Sci. Technol.* **9**, 163–168.

STIMSON, M. & JEFFERY, G.B. 1926 The motion of two spheres in a viscous fluid. *Proc. R. Soc. Lond.* A **111** (757), 110–116.

TAYLOR, G.I. 1962 On scraping viscous fluid from a plane surface. In *Miszellaneen der Angewandten Mechanik* (ed. M. Schäfer), pp. 313–315. Akademie-Verlag.

VOLPE, A., PAIÈ, P., ANCONA, A., OSELLAME, R., LUGARÀ, P.M. & PASCAZIO, G. 2017 A computational approach to the characterization of a microfluidic device for continuous size-based inertial sorting. *J. Phys. D* **50** (25), 255601.

WANG, Z. & ZHE, J. 2011 Recent advances in particle and droplet manipulation for lab-on-a-chip devices based on surface acoustic waves. *Lab on a Chip* **11** (7), 1280–1285.

WU, H., ROMANÒ, F. & KUHLMANN, H.C. 2021 Attractors for the motion of a finite-size particle in a two-sided lid-driven cavity. *J. Fluid Mech.* **906**, A4.

YAHIAOUI, S. & FEUILLEBOIS, F. 2010 Lift on a sphere moving near a wall in a parabolic flow. *J. Fluid Mech.* **662**, 447.

YANG, F.-L. 2010 A formula for the wall-amplified added mass coefficient for a solid sphere in normal approach to a wall and its application for such motion at low Reynolds number. *Phys. Fluids* **22** (12), 123303.